# Utilizing photocorrosion-recrystallization to prepare a highly stable and efficient CdS/WS$_2$ nanocomposite photocatalyst for hydrogen evolution

Yueyao Zhong, Gang Zhao, Fukun Ma, Yongzhong Wu*, Xiaopeng Hao*

*State Key Lab. of Crystal Materials, Shandong University, Jinan 250100, China*

ABSTRACT

Efficiency and stability are the two key elements for photocatalyst. The application of CdS, as a classical photocatalyst, has been seriously restricted because of the inherent photocorrosion issue. Based on the rate-theory analysis, in this paper, we propose the photocorrosion and recrystallization of CdS on the surface of WS$_2$ nanosheets under visible light irradiation to resolve the photocorrosion issue. A highly stable and efficient CdS/WS$_2$ photocatalyst has been obtained following this strategy for the first time. The rate of H$_2$ evolution distinctly increases (56.2 times) compared with that in pure CdS nanoparticles, and keeps excellent stability in hydrogen generation for more than 200 h without any decrease, which are superior to any other previously reported CdS based photocatalysts. This new approach has potential application in designing and fabricating more stable and efficient composite chalcogenide photocatalysts.

© 2016 Elsevier B.V. All rights reserved.

## 1. Introduction

Given the shortage in energy resources and the worsening environmental pollution, converting solar energy into chemical energy in the form of hydrogen fuel, which is both clean and renewable, has become a highly appealing process [1]. Among the methods used to achieve this process, photocatalytic H$_2$ evolution (PHE) by water splitting using semi-conductive photocatalystshas received considerable attention [2,3]. Recent works in this area have focused on developing visible-light-responsive photocatalysts, because visible light contributes approximately 43% of solar radiation energy, whereas ultraviolet (UV) light accounts for only approximately 4% [4]. Among semi-conductive photocatalysts, CdS has been extensively studied, because its band gap of approximately 2.4 eV matches well with the visible spectral range of solar irradiation [5]. However, CdS nanoparticles have low photo-stability, and high recombination rate of photo-induced electron-hole pairs. For the sake of demonstrating the extreme effect of CdS during photocatalysis, copious impressive results have been achieved by extension of the surface area as a tuning crystal structure (e.g. CdS nanowires, netted sphere-like CdS nanostructures) [6,7], syntheses of heterostructures [8–11], and core-shell nanoparticles [12]. But the enhancement of catalytic efficiency in these CdS related catalysts are still prerequisite.

Increasing attention has been given to the important roles of cocatalysts in photocatalytic and photoelectrochemical water splitting reactions. For example, Qin Li and co-workers decorated graphene nanosheets with CdS clusters as visible-light-driven photocatalysts [13]. Can Li and co-workers loaded MoS$_2$ as cocatalyst on CdS for photocatalytic H$_2$ production under visible light [14,15]. Jinhua Ye and co-workers fabricated a nanosized layer-structured MoS$_2$/graphene nanosheet loaded with CdS nanoparticles with a 3D hierarchical configuration and investigated its hydrogen production activities under visible light [16]. Loading cocatalysts on semiconductors can facilitate reactions by providing active sites/reaction sites while suppressing charge recombination and reverse reactions. Cocatalysts can also improve the photostability of catalysts through the timely consumption of photogenerated charges, particularly holes [17]. WS$_2$ and MoS$_2$ have extremely similar crystal structures and chemical properties. Moreover, WS$_2$ and MoS$_2$ are active components in many PHE processes [18–21]. It has been found that the band structure of the WS$_2$ nanosheets (which consist of less than 5 monolayers) undergoes indirect-to-direct gap transition when the nanosheets are reduced to a single monolayer [22]. Can Li and co-workers determined that WS$_2$ could also act as a cocatalyst similar to MoS$_2$ for CdS in photocatalytic H$_2$ production, and it could function as an efficient cocatalyst with a capability comparable with those of Pt, Rh, Ru, and Au noble metals [23].

Researchers also fabricated $MS_2$-CdS (M = W or Mo) nanohybrids as photocatalyst in hydrogen evolution reaction [24,25].

Considerable efforts have been exerted on CdS based photocatalysts for PHE, howbeit, the CdS based photocatalysts showed low photocatalytic performances and stabilities toward PHE under visible light irradiation (>420 nm), because of the photocorrosion issue, which is inevitable. In this study, we proposed the photocorrosion and recrystallization of CdS on the surface of $WS_2$ nanosheets under irradiation to resolve the photocorrosion issue for the first time. Besides, the mechanism of the separation of electron-hole pairs, and reduction of the probability of photogenerated charge recombination in $CdS/WS_2$ nanocomposites during irradiation were also mentioned. It is expected that this work can open up new frontier for advancing the utilization of photocorrosion-recrystallization to synthesize highly stable and efficient photocatalysts.

## 2. Experimental section

### 2.1. Materials

Tungsten disulfides ($WS_2$, 99%) were purchased from Shanghai Macklin Biochemical Co. Ltd. (Shanghai, China). Cadmium thiocyanate ($Cd(SCN)_2$), ethanol, ethanediol and lactic acid were purchased from Sinopharm Chemical Reagent Co. Ltd. (Shanghai, China). 1-Butyl-3-methylimidazolium thiocyanate ([BMIM]■SCN) was purchased from Shanghai Chengjie Chemical Co. Ltd. (Shanghai, China). All reagents were used as received without further treatment. Solutions were freshly prepared with deionised water.

### 2.2. Synthesis of CdS/WS₂ nanocomposites

The $WS_2$ nanosheets were prepared by ball-milling. $CdS/WS_2$ composites were prepared according to our previous work [36]. A certain weight of $WS_2$ nanosheets was dissolved in 30 mL of ethanediol with 0.343 g of $Cd(SCN)_2$ and 0.285 mL of [BMIM]■SCN. After all reagents were dissolved, the solution was added to polytetrafluoroethylene-lined autoclaves of a microwave digestion system. The autoclaves were maintained at 180 °C for 30 min. After cooling to room temperature, the precipitate was filtered and washed with ethanol and water several times. Finally, $CdS/WS_2$ nanocomposites with a certain amount of $WS_2$ were obtained through vacuum drying at 40 °C for 6 h.

### 2.3. Characterizations

TEM and HRTEM images were obtained with a Philips Tecnai 20U-Twin microscope at an acceleration voltage of 200 kV. SEM images were obtained with a Hitachi S-4800 field-emission scanning electron microscope. XPS (Thermo ESCALAB 250) was performed using monochromated Al Kα radiation (1486.8 eV). XRD patterns were obtained on a Bruker D8 advance X-ray diffractometer with Cu–Kα radiation ($\lambda$ = 0.15418 nm). UV–vis DRS results were obtained with a Shimadzu UV2550 recording spectrophotometer equipped with an integrating sphere from 200 to 800 nm. $BaSO_4$ is used as reference. AFM images were obtained with a Nanoscope Multi Mode V instrument (Digital Instrument/Bruker Systems), operated in Scan Asyst Air mode. Inductively coupled plasma-atomic emission spectrometry (ICP-AES) were obtained with IRIS INTREPID II ICP-AES.

### 2.4. Photocatalytic activity measurement

The photocatalytic reactions are carried out in a Pyrex reaction cell connected to a closes gas circulation an evacuation system. 0.1 g catalyst is dispersed in 100 mL aqueous solution containing 20 mL lactic acid as sacrificial agent. Then the suspension be thoroughly

degassed and irradiated by a Xe lamp (300 W) equipped with an optical cut off filter ($\lambda$ > 420 nm) to eliminate ultraviolet light. The temperature of the reactant solution is maintained at 279 K by flowing cooling water during the reaction. The amount of $H_2$ produced is analysed using an online gas chromatography (Gc7900 Tianmei Shanghai China). The activities of different catalysts are compared using the average rate of $H_2$ evolution in the first 5 h.

### 2.5. Photoelectrochemical activity measurements

PEC test systems contain a CHI660D workstation (Shanghai Chenhua, China) with a three-electrode configuration using the prepared samples as the working electrodes, a Pt plate as the counter electrode, Ag/AgCl as the reference electrode and a 300 W Xe lamp equipped with an optical cut off filter ($\lambda$ > 420 nm) as the light source. $Na_2SO_4$ aqueous solution (0.5 M) is used as the electrolyte. The working electrodes are prepared as follows: 10 mg the as-prepared nanocomposites are dispersed in absolute ethanol and the suspension is directly deposited onto an FTO conductive glass plate and then dry at 80 °C in a vacuum oven.

## 3. Results and discussion

### 3.1. Morphology and structure characterization of preliminary CdS/WS₂ nanocomposites

In recent years, noble-metal-free cocatalyts have attracted increasing attention, particularly $WS_2$ and $MoS_2$ [24,25]. Herein, the derived nanosheets are characterized in S1-S3, Supplementary Information. Fig. 1a presents the morphology of the preliminary $CdS/WS_2$ nanocomposites (freshly synthesized without irradiation) with numerous small CdS nanospheres uniformly spread on the surface of the $WS_2$ nanosheets. Compared with pure CdS nanoparticles (see Fig. S1b), average diameter decreased to 50 nm, which increased the specific surface area. The result was confirmed by BET (see S6, Supplementary information). The surface area of the as-prepared $CdS/WS_2$ nanocomposites is 26.02 $m^2$ $g^{-1}$. It is larger than that of pure CdS nanoparticles (18.96 $m^2$ $g^{-1}$). The inset shows the transmission electron microscopy (TEM) image of the $CdS/WS_2$ nanocomposites, which is well tallied with the SEM results. The present CdS spheres have a crumbly structure that consists of small particles, which is beneficial for promoting the absorbability of CdS as a photocatalyst. To further study the junction formation between CdS nanoparticles and $WS_2$ nanosheets, high-resolution TEM (HRTEM) analysis was also employed. Fig. 1b shows HRTEM image of the $CdS/WS_2$ nanocomposites. It can be clearly seen, the presence of both CdS planes and $WS_2$ nanosheets planes. Fig. 1b also indicates that junctions exist between CdS nanoparticles, and $WS_2$ nanosheets, not only the mixture of these two components. Furthermore, S7, Supplementary Information indicates that contact occurs between $WS_2$ nanosheets and CdS nanoparticles in the $CdS/WS_2$ nanocomposites and such contact is favorable for the separation of charge between these two components.

The X-ray diffraction (XRD) patterns (Fig. 1c) indicate that $WS_2$ nanosheets consist of hexagonal-phase $WS_2$ (JCPDS no.08-0237) with several layers (see S2 and S3, Supplementary information), CdS nanoparticles consist of hexagonal-phase CdS (JCPDS no.41-1049), and the as-prepared $CdS/WS_2$ nanocomposites with well-defined crystalline consist of hexagonal-phase $WS_2$ nanosheets and CdS. X-ray photoelectron spectroscopy (XPS) is a particularly useful tool for studying the composition and electronic structure of the surface of materials. It can also provide information regarding the chemical environment of the elements in composites. XPS was used to investigate the chemical states of Cd, W, and S species in the as-prepared $CdS/WS_2$ nanocomposites. The high-
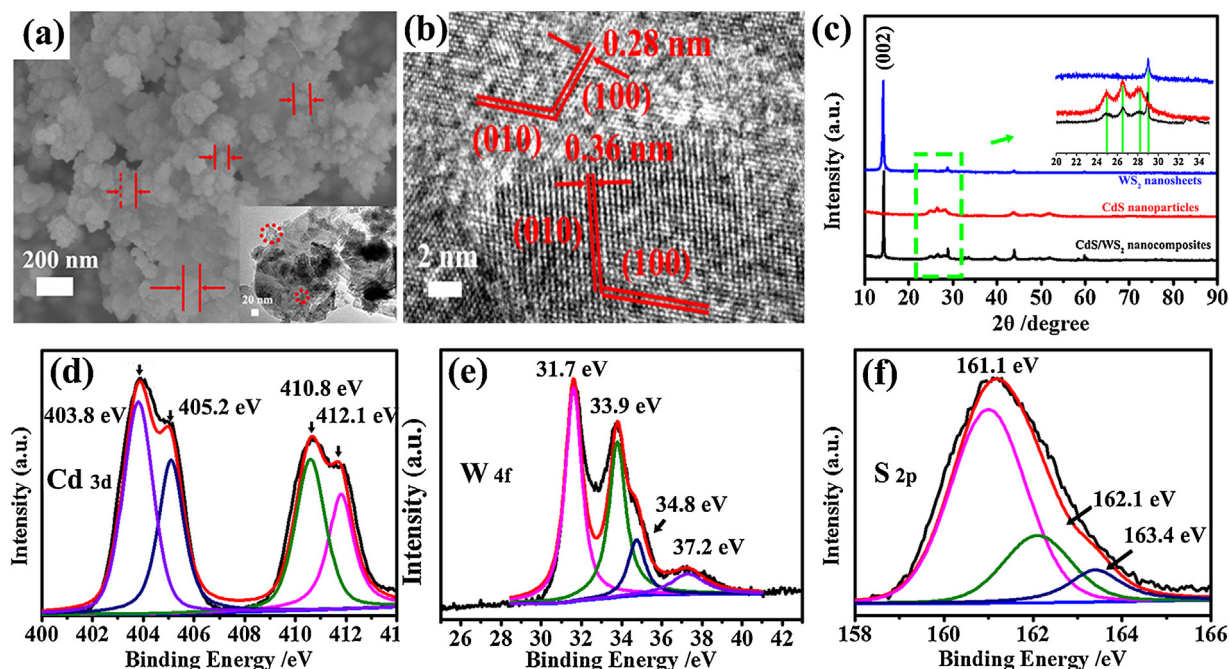
**Fig. 1.** Morphology of the preliminary CdS/WS₂ nanocomposites (the amount of WS₂ nanosheets is 40 wt%). (a) SEM image of the CdS/WS₂ nanocomposites. The inset shows TEM image of CdS/WS₂ nanocomposites. (b) HRTEM image of the 40 wt% CdS/WS₂ nanocomposites. (c) XRD patterns of WS₂ nanosheets, pure CdS nanoparticles, and the preliminary CdS/WS₂ nanocomposites. (d) High-resolution XPS spectrum of the Cd3d region. (e) High-resolution XPS spectrum of the W4f region. (f) High-resolution XPS spectrum of the S2p region.

resolution XPS of Cd 3d (Fig. 1d) exhibits four peaks at 403.8 eV, 405.2 eV, 410.8 eV and 412.1 eV, respectively. The peaks at 403.8 eV and 410.8 eV are in accordance with the peaks of Cd 3d in pure CdS nanoparticles (see S4, Supplementary Information). The peaks at 405.2 eV and 412.1 eV indicate the combination of CdS and WS₂ nanosheets. The high-resolution XPS of W 4f and S 2p also indicate this. Compared with the W 4f binding energy (BE) peaks in pure WS₂ nanosheets (33.4 eV and 35.5 eV in S5, Supplementary Information), the W 4f peaks in CdS/WS₂ nanocomposites are at 31.7 eV and 33.9 eV (Fig. 1e). The peak at 37.2 eV belongs to W 5p3. Fig. 1f shows the XPS spectrum of the S 2p region in CdS/WS₂ nanocomposites, which can be fitted into three peaks at 161.1 eV, 162.1 eV, and 163.4 eV. Compared with S 2p BE in pure CdS nanoparticles (160.8 eV, 162.1 eV and 163.1 eV in S4, Supplementary information) and pure WS₂ NSs (163 eV and 164.1 eV in S5, Supplementary information), this also indicates the combination of CdS and WS₂ NSs.

### 3.2. Photocatalytic H₂ evolution activities

Fig. 2 shows the photocatalytic H₂ production activities of pure CdS nanoparticles, the CdS/WS₂ nanocomposites with different weight amounts of WS₂ nanosheets, WS₂ nanosheets in lactic acid solution, and the photocatalytic stability of the CdS/WS₂ nanocomposites. As shown in Fig. 2a, when pure CdS nanoparticles used as catalyst in lactic acid solution, the amount of H₂ produced remain low, because of the fast recombination of electron–hole pairs. Moreover, no H₂ is detected when only WS₂ nanosheets are used as catalyst, which suggests that WS₂ nanosheets are inactive for PHE. With the increasing of WS₂ nanosheets, the amount of H₂ evolution initially increases step by step, and then achieves a maximum value, when the added amount of WS₂ nanosheets is approximately 40%. Further adding WS₂ nanosheet results a decrease in PHE. Excessive WS₂ nanosheets can prevent light from reaching the surface of the CdS photocatalysts. WS₂ nanosheets may absorb some visible light, and thus, led to a light-harvesting

competition between CdS nanoparticles and WS₂ nanosheets with increasing WS₂ nanosheet content. Such competition can deteriorate photocatalytic performance. Fig. 2b shows the rate of H₂ evolution for the CdS/WS₂ catalysts with different amounts of WS₂ nanosheets. Pure CdS nanoparticles exhibit low activity for PHE with 6.65 μmol h⁻¹ g⁻¹. After adding only 10 wt% WS₂ nanosheets, the rate of H₂ evolution in the CdS/WS₂ nanocomposites increases to 116.01 μmol h⁻¹ g⁻¹, which is 17.45 times higher than that in pure CdS nanoparticles. Meanwhile, by adding 40 wt% WS₂ nanosheets, the rate of H₂ evolution in the CdS/WS₂ nanocomposites increases to 373.41 μmol h⁻¹ g⁻¹, which is 56.15 times higher than that in pure CdS nanoparticles. To investigate the stability of the CdS/WS₂ nanocomposites, photocatalytic reaction was conducted for 40 repeated cycles, and the system was enhanced every 5 h. As shown in Fig. 2c the rate of H₂ evolution in the as-prepared 40 wt% CdS/WS₂ nanocomposites increases with each reaction cycle until irradiation for 100 h is completed. This rate corresponds to an apparent quantum efficiency of 25.03% ($\lambda_{ex}$ = 420 nm) (see S9, Supplementary Information). Fig. 2d shows that the final CdS/WS₂ nanocomposite (after irradiation for 200 h) demonstrates high stability after 200 h photocatalytic reaction, with nearly no activity loss. These results validate the excellent activity and superb stability of the as-obtained CdS/WS₂ nanocomposites.

### 3.3. Mechanism of photocatalysis for PHE

From the above photocatalytic H₂ evolution activities, we can see that CdS/WS₂ nanocomposites exhibit excellent catalytic effects over CdS nanoparticles for PHE. Importantly, CdS/WS₂ nanocomposites are much more photostability than CdS nanoparticles. Thus, why does the catalytic activity of H₂ evolution improve every 5 h, up to 100 h? We will explain the mechanism in the following three aspects: nanostructure, theoretical analysis, and electron energy levels.
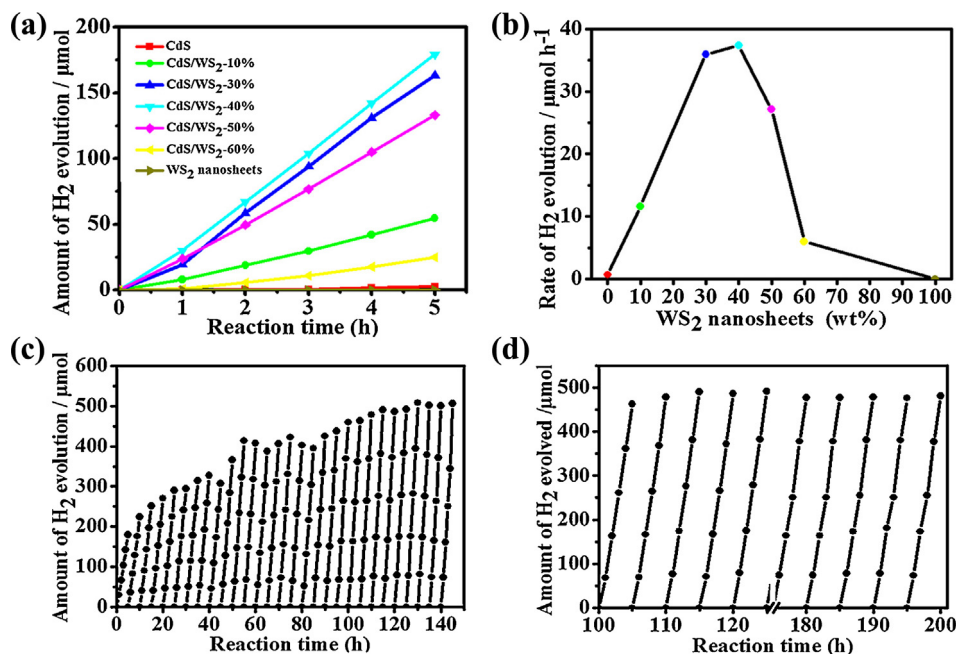
**Fig. 2.** (a) $H_2$ evolution of different samples with varying weight amounts of $WS_2$ nanosheets and cycling behavior in 5 h. (b) $H_2$ evolution rates of pure CdS nanoparticles, CdS/$WS_2$ nanocomposites, and $WS_2$ nanosheets. (c, d) $H_2$ evolution during the photocatalytic stability study. Conditions: 0.1 g CdS/$WS_2$ nanocomposites, 100 mL aqueous solution with 20 mL lactic acid, and 300 W Xe lamp with an optical cut off filter ($\lambda > 420$ nm).
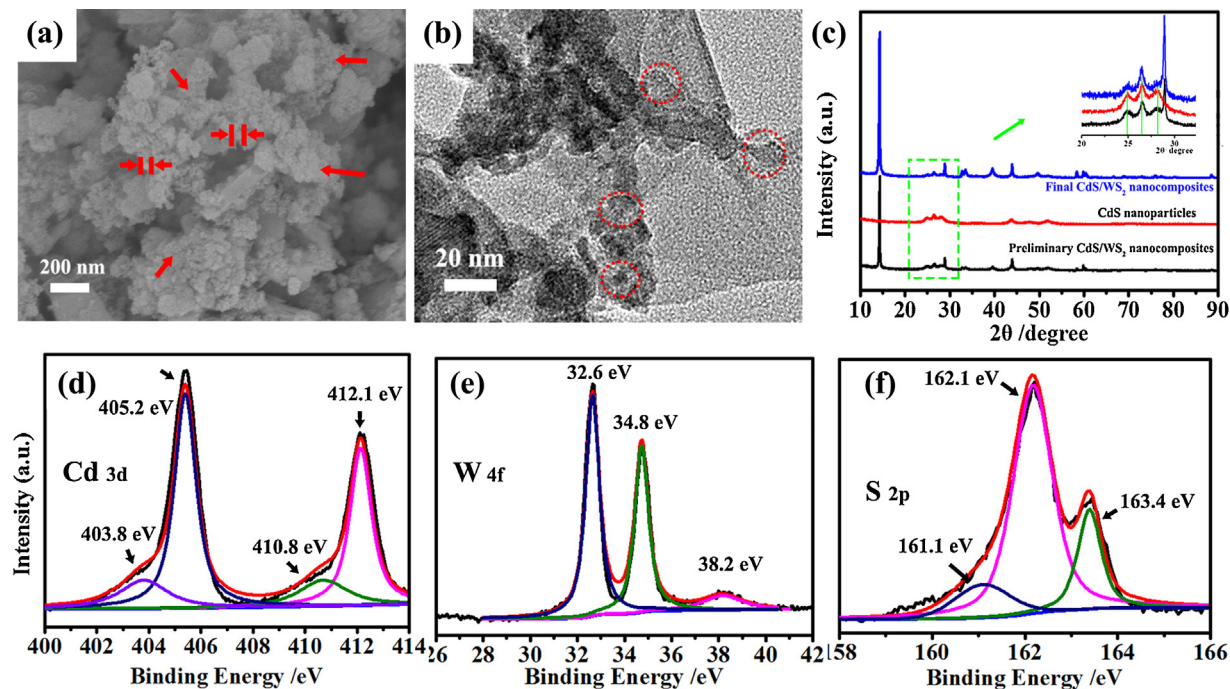


**Fig. 3.** Morphology of the Final CdS/$WS_2$ nanocomposites (the amount of $WS_2$ nanosheets is 40 wt% after irradiation for 200 h). (a) SEM image of the final CdS/$WS_2$ nanocomposites. (b) TEM image of the final CdS/$WS_2$ nanocomposites. (c) XRD patterns of CdS nanoparticles, preliminary CdS/$WS_2$ nanocomposites, and final CdS/$WS_2$ nanocomposites. (d) High-resolution XPS spectrum of the Cd3d region. (e) High-resolution XPS spectrum of the W4f region. (f) High-resolution XPS spectrum of the S2p region.

### 3.3.1. From nanostructure

To investigate whether the phase structure of the final CdS/$WS_2$ nanocomposites has changed or not, the morphology and structure characterizations of the final CdS/$WS_2$ nanocomposites are shown in Fig. 3. The images of the final CdS/$WS_2$ nanocomposites after being irradiated for 200 h are shown in Fig. 3a and b, where the average size of CdS nanoparticles is approximately 20 nm. The final nanocomposites differ slightly from the preliminary products and

have smaller and denser CdS nanoparticles on the surface of $WS_2$ nanosheets. This means that CdS nanoparticles in minor size are beneficial for PHE. Fig. 3c shows the XRD patterns of CdS nanoparticles, preliminary CdS/$WS_2$ nanocomposite, and final CdS/$WS_2$ nanocomposites. The XRD patterns show that there are no differences between the preliminary CdS/$WS_2$ nanocomposite and the final CdS/$WS_2$ nanocomposites, which means that illumination does not change the crystalline structure of CdS/$WS_2$ nanocompos-

ites. Fig. 3d–f shows the high-resolution XPS spectra of Cd 3d, W 4f, and S 2p in final CdS/WS$_2$ nanocomposites. Compared with high-resolution XPS spectra in preliminary CdS/WS$_2$ nanocomposite (Fig. 1d), the peak intensities of Cd 3d in final CdS/WS$_2$ nanocomposites at 403.8 eV and 410.8 eV decrease and the peak intensitied at 405.2 eV and 410.8 eV increase. Fig. 3e shows W 4f peak at 32.6 eV and 34.8 eV. Compared with the BE of W 4f in preliminary CdS/WS$_2$ nanocomposites (Fig. 1e), the BE of W 4f peaks in final CdS/WS$_2$ nanocomposites shift to high. Compared with the BE of W 4f in WS$_2$ nanosheets (see S5, Supplementary Information), the BE of W 4f peaks in final CdS/WS$_2$ nanocomposites shift to low. Fig. 3f shows the S 2p region of final CdS/WS$_2$ nanocomposites. Compared with S 2p region in preliminary CdS/WS$_2$ nanocomposites (Fig. 1f), the peak intensity at 161.1 eV decreases. The peak intensity at 162.1 eV increases and the peak intensity at 163.4 eV increases, respectively. The CdS particles in preliminary CdS/WS$_2$ nanocomposites are corroded by light irradiation. Then, Compared with pure CdS particles and WS$_2$ nanosheets, the peak intensities of Cd 3d and S 2p in final CdS/WS$_2$ nanocomposites decrease, meanwhile, the peak intensities of W 4f and S 2p in final CdS/WS$_2$ nanocomposites increased. These results indicate the photocorrosion- recrystallization process of CdS/WS$_2$ nanocomposites.

### 3.3.2. From theoretical analysis

S-vacancies are active sites for further reactions. The stoichiometric ratio of the nanosheet was determined using the XPS spectra. The atomic ratio of WS$_2$ nanosheets was S/W = 1.89 (See S5, Supplementary information). This implies that there are many defects (including S-vacancies) on the surface of WS$_2$ nanosheets. There are two reasonable explanations for S-vacancy of WS$_2$: (1) in the exfoliation process, a small amount of W-S bonds rupture can result in forming S-vacancy in the edge of WS$_2$ and (2) obtained WS$_2$ nanosheets are very thin layer, the activity of nanosheets is higher than that of bulk WS$_2$. Sulfur ions may produce hydrolysis reaction with water. Thus, WS$_2$ nanosheets surfaces contain large amounts of S-vacancy [27]. The S-vacancies in WS$_2$ nanosheets provide a low barrier to the initial formation of the new phase [28]. S-vacancies are tending to absorb S$^{2-}$ to modify and eliminate the defects [29]. Although CdS nanoparticles are blended into WS$_2$ nanosheets in the preliminary CdS/WS$_2$ nanocomposites, the size of CdS nanoparticles in these nanocomposites is not optimal for a photocatalytic reaction (Fig. 1a), because of the fast growth rate. Photocorrosion is known to occur in CdS reaction (CdS + H$_2$O → H$_2$ + Cd$^{2+}$ + S + 2OH$^-$) in the absence of oxygen [30], however, photocorrosion in CdS is negligibly small when lactic acid is used as a sacrificial agent [31]. During irradiation, a reversible reaction takes place: CdS ⇌ Cd$^{2+}$ + S$^{2-}$ [32]. The concentration of Cd$^{2+}$ and S$^{2-}$ increased in the solvent, with the increase of illumination time, and reached to 180.5 ppm and 61.67 ppm, respectively, after irradiation for 120 h. (Fig. 4a) During irradiation, large-size CdS dissolves to Cd$^{2+}$ and S$^{2-}$ in CdS/WS$_2$ nanocomposites, and the S$^{2-}$ are easy to reach and connect with the active sites in S-vacancies. Based on the rate-theory analysis of surface roughness, the recrystallization process rate of CdS is slow which results in small and uniformed CdS nanoparticles [28]. Consequently, CdS nanoparticles cover in the surface of WS$_2$ nanosheets with small size (Fig. 3a). Furthermore, after recycling for 100 h, the dissolution and formation of CdS achieves equilibrium state, and the H$_2$ evolution rate reaches its maximum value and remains unchanged (Fig. 2d). Those results are in accord with the inductively coupled plasma-atomic emission spectrometry (ICP-AES) results: the concentration of Cd$^{2+}$, S$^{2-}$, and W$^{4+}$ are reached to 51.52 ppm, 12.66 ppm and 15.12 ppm in the solvent, respectively, after irradiation for 90 h (Fig. 4b). Compared with pure CdS nanoparticles, the concentration of those ions are lower, and reach to equilibrium state after irradiation for 90 h. The mechanism might be as follows: CdS dissolves to Cd$^{2+}$ and S$^{2-}$ under the

irradiation, and the concentration increase with the illumination time. When concentration of Cd$^{2+}$ and S$^{2-}$ reach a certain value, it will trigger the recrystallization process of CdS on the S-vacancies of WS$_2$ nanosheets until reaching the equilibrium state. The photocorrosion and recrystallization process of CdS/WS$_2$ nanocomposites is schematically described in Fig. 4c.

### 3.3.3. From electron energy levels

The results of the UV–vis diffuse reflectance spectroscopy (UV–vis DRS) on CdS nanoparticles, WS$_2$ nanosheets, the preliminary CdS/WS$_2$ nanocomposites, and the final CdS/WS$_2$ nanocomposites are shown in Fig. 5a. As a well-known visible-light-induced photocatalyst, pure CdS nanoparticles absorb visible light with wavelengths less than 520 nm, which matches the theoretical band gap of 2.4 eV. By adding WS$_2$ nanosheets, the absorption wavelength red shifts, because of the narrow bandgap of WS$_2$ nanosheets [33]. The bandgap of bulk WS$_2$ is 1.35 eV. With the increase of WS$_2$ thickness, the conduction band (CB) minimum/valence band (VB) maximum decreases/increases, and that leads to a narrowing band gap. This finding is consistent with the experimental results [34]. In addition, the final CdS/WS$_2$ nanocomposites exhibit the same absorption peak as that of the preliminary nanocomposites. However, intensity is enhanced, which conforms to the BET measurement. The surface area of the final CdS/WS$_2$ nanocomposites (53.39 m$^2$ g$^{-1}$) is larger than that of the preliminary CdS/WS$_2$ nanocomposites. (See S6, Supplementary information) The purple line indicates good light absorption and perfect stability after visible light irradiation of the final CdS/WS$_2$ nanocomposites, which is beneficial for PHE.

As mentioned in the introduction, WS$_2$ is a good H$_2$ evolution catalyst. Thus, it is important for us to investigate the effect of band gap and CB position on the synergistic influence between CdS nanoparticles and WS$_2$ nanosheets.

Based on the preceding results, a proposed mechanism for photocatalytic H$_2$ production in the CdS/WS$_2$ nanocomposites is presented in Fig. 5b. The electronic structure of WS$_2$ nanosheets is provided in S8, Supplementary Information. The VB position of WS$_2$ nanosheets was 1.18 eV. Upon photo-excitation, electron-hole pairs are produced in the VB and CB of CdS nanoparticles, respectively. The same process occurs in WS$_2$ nanosheets. The electrons in the CB of CdS nanoparticles transfer to the CB of WS$_2$ nanosheets, and finally to produce H$_2$. The holes are consumed by lactic acid. Meanwhile, photo-generated holes can also transfer stepwise from the VB of CdS nanoparticles to the VB of WS$_2$ nanosheets and accumulate for oxidation process [35]. Consequently, the probability of photogenerated charge recombination considerably decreases. Numerous photogenerated electrons are available to reduce H$^+$ to H$_2$, which results in a highly efficient PHE activity. The preceding discussions explain why the H$_2$ evolution rate of the CdS/WS$_2$ nanocomposites increases and exhibits excellent stability in photocatalytic reaction after being irradiated by visible light for 100 h.

The minor sized CdS nanoparticles are beneficial for the injecting of photogenerated electrons from CdS into the WS$_2$ nanosheets. This also can be further confirmed by transient photocurrent experiments in Fig. 5c and d. As shown in Fig. 5c, compared with that of CdS, WS$_2$, and P-CdS/WS$_2$/FTO, the current intensity of F-CdS/WS$_2$/FTO is considerably higher. For a distinct comparison, the photo-generated current-time curves of CdS, WS$_2$, and P-CdS/WS$_2$/FTO within a small range scale are shown in Fig. 5d. The photocurrent is mainly determined by the separation efficiency of electron–hole pairs within the photoelectrodes [26]. When the light is on, the photo-generated electrons and holes move in the opposite directions to weaken electric field strength and the generated current. When the light is off, this effect gradually diminishes with the recombination of electrons and holes, and the current decreases.
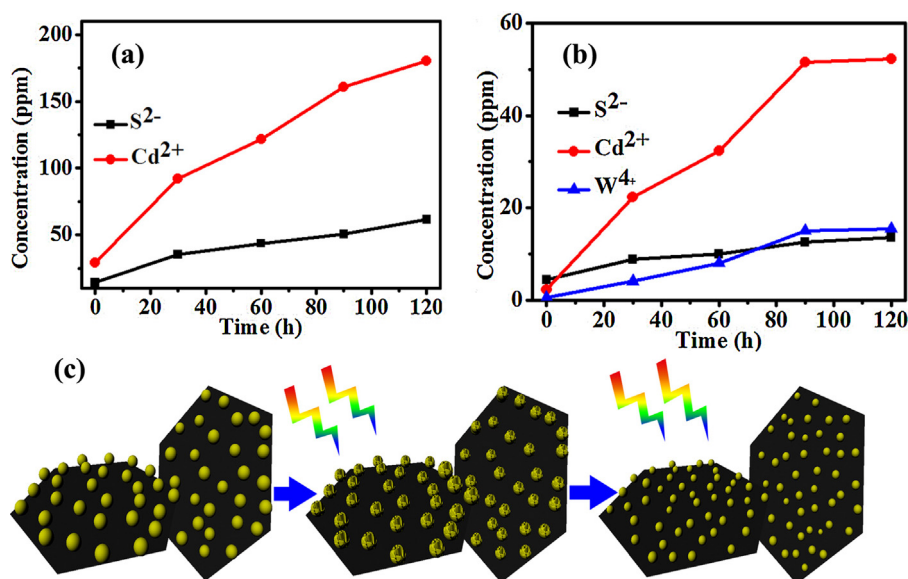
**Fig. 4.** (a) The concentration of $S^{2-}$ and $Cd^{2+}$ decomposed from CdS nanoparticles during the irradiation. (b) The concentration of $S^{2-}$, $Cd^{2+}$, and $W^{4+}$ decomposed from $CdS/WS_2$ nanocomposites during the irradiation. (ICP-AES Condition: Sampling at different times and centrifuged to remove the photocatalyst powder). (c) Schematic of CdS photocorrosion and recystallization on the surface of $WS_2$ nanosheets.
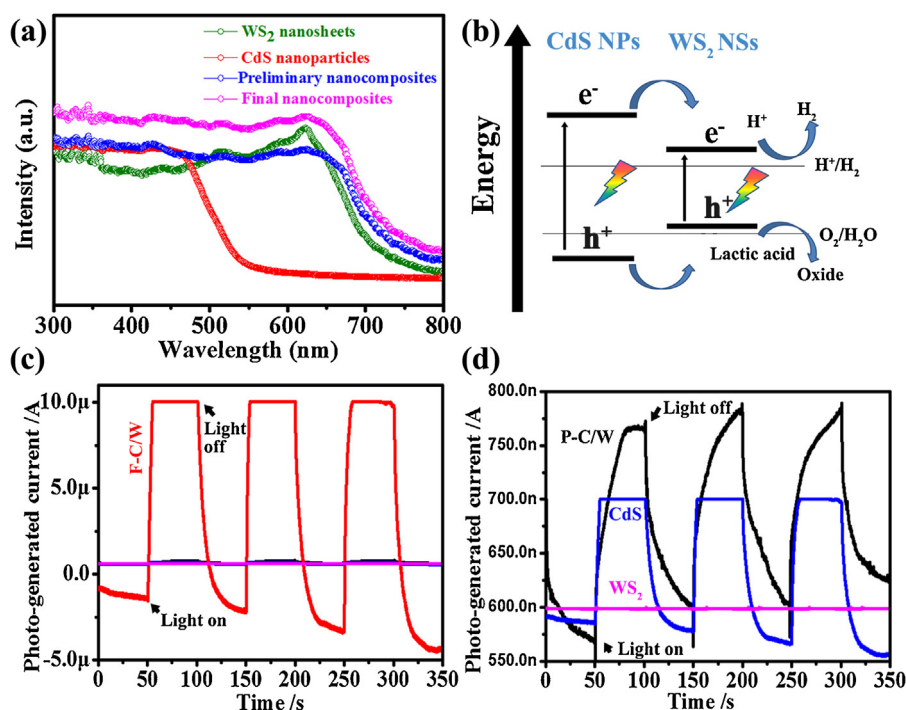


**Fig. 5.** (a) UV–vis DRS on CdS nanoparticles, $WS_2$ nanosheets, the preliminary $CdS/WS_2$ nanocomposites, and the final $CdS/WS_2$ nanocomposites. (b) Schematic of charge separation and transfer in the $CdS/WS_2$ nanocomposites under visible light. (c) Photocurrent responses (-0.33 V bias) of the as-prepared $P-CdS/WS_2/FTO$ and $F-CdS/WS_2/FTO$ electrodes in 0.5 M $Na_2SO_4$ solution under visible light. (d) Photo-generated current-time curve of $P-CdS/WS_2/FTO$ within a small range scale. (The amount of $WS_2$ nanosheets is 40 wt%, P means preliminary, F means final).

## 4. Conclusion

In summary, $CdS/WS_2$ nanocomposites have been prepared via a simple microwave-assisted method at first, and then the highly stable and efficient $CdS/WS_2$ nanocomposite photocatalysts were prepared with the help of photocorrosion-recrystallization process. By optimizing each component proportion, the $CdS/WS_2$ nanocomposites exhibited the highest PHE activity when the weight ratio of

$WS_2$ nanosheets was 40 wt%. PHE activity was tested in a lactic acid solution that corresponded to a QE of 25.03% at 420 nm. These characterizations demonstrated that photocorrosion-recrystallization process led to the high photocatalytic activity and excellent photocatalytic stability of the $CdS/WS_2$ nanocomposites for PHE. Utilizing the photocorrosion-recrystallization to prepare highly stable and efficient photocatalyst is expected to have potential applications in photocatalytic reactions.

## Acknowledgment

## Appendix A. Supplementary data

Supplementary data associated with this article can be found, in the online version, at http://dx.doi.org/10.1016/j.apcatb.2016.06.065.

## References

[1] F. Fresno, R. Portela, S. Suárez, J.M. Coronado, J. Mater. Chem. A 2 (2014) 2863–2884.
[2] J. Liu, Y. Liu, N.Y. Liu, Y.Z. Han, X. Zhang, H. Huang, Y. Lifshitz, S.T. Lee, J. Zhong, Z.H. Kang, Science 347 (2015) 970–974.
[3] H. Zhang, X.J. Lv, Y.M. Li, Y. Wang, J.H. Li, ACS Nano 4 (2009) 380–386.
[4] Y.H. Zhang, N. Zhang, Z.R. Tang, Y.J. Xu, ACS Nano 6 (2012) 9777–9789.
[5] A.H. Ye, W.Q. Fan, Q.H. Zhang, W.P. Deng, Y. Wang, Catal. Sci. Technol. 2 (2012) 969–978.
[6] C. Ye, G. Meng, Y. Wang, Z. Jiang, L. Zhang, J. Phys. Chem. B 106 (2002) 10338–10341.
[7] P.T. Zhao, K.X. Huang, Cryst. Growth Des. 8 (2007) 717–722.
[8] N.N. Hewa-Kasakarage, M. Kirsanova, A. Nemchinov, N. Schmall, P.Z. El-Khoury, A.N. Tarnovsky, M. Zamkov, J. Am, Chem. Soc. 131 (2009) 1328–1334.
[9] K. Wu, H. Zhu, Z. Liu, W. Rodriguez-Cordoba, T. Lian, J. Am. Chem. Soc. 134 (2012) 10337–10340.
[10] L. Wang, W.Z. Wang, CrystEngComm 14 (2012) 3315–3320.
[11] M. Reza Gholipour, C.T. Dinh, F. Beland, T.O. Do, Nanoscale 7 (2015) 8187–8208.
[12] J. Frenzel, S. Thieme, G. Seifert, J.O. Joswig, J. Phys. Chem. C 115 (2011) 10338–10344.
[13] Q. Li, B.D. Guo, J.G. Yu, J.R. Ran, B.H. Zhang, H.J. Yan, J.R. Gong, J. Am. Chem. Soc. 133 (2011) 10878–10884.
[14] X. Zong, H.J. Yan, G.P. Wu, G.J. Ma, F.Y. Wen, L. Wang, C. Li, J. Am, Chem. Soc. 130 (2008) 7176–7177.
[15] X. Zong, G.P. Wu, H.J. Yan, G.J. Ma, J.Y. Shi, F.Y. Wen, L. Wang, C. Li, J. Phys. Chem. C 114 (2010) 1963–1968.
[16] K. Chang, Z.W. Mei, T. Wang, Q, Kang, S.X. Ouyang, J.H. Ye, ACS Nano 8 (2014) 7078–7087.
[17] J.H. Yang, D.G. Wang, H.X. Han, C. Li, Acc. Chem. Res. 46 (2013) 1900–1909.
[18] B. Mahler, V. Hoepfner, K. Liao, G.A. Ozin, J. Am. Chem. Soc. 136 (2014) 14121–14127.
[19] J.J. Wang, Z.Y. Guan, J. Huang, Q.X. Li, J.L. Yang, J. Mate, Chem. A 2 (2014) 7960–7966.
[20] Q. Xiang, J. Yu, M. Jaroniec, J. Am, Chem. Soc. 134 (2012) 6575–6578.
[21] H. Zhao, Y.M. Dong, P.P. Jiang, H.Y. Miao, G.L. Wang, J.J. Zhang, J. Mate, Chem. A 3 (2015) 7375–7381.
[22] W.J. Zhao, Z. Ghorannevis, L.Q. Chu, M.L. Toh, C. Kloc, P.H. Tan, G. Eda, ACS Nano 7 (2012) 791–797.
[23] X. Zong, J.F. Han, G.J. Ma, H.J. Yan, G.P. Wu, C. Li, J. Phys. Chem. C 115 (2011) 12202–12208.
[24] J.Z. Chen, X.J. Wu, L.S. Yin, B. Li, X. Hong, Z.X. Fan, B. Chen, C. Xue, H. Zhang, Angew. Chem. Int. Ed. 54 (2015) 1210–1214.
[25] K. Chang, M. Li, T. Wang, S. Ouyang, P. Li, L.Q. Liu, J.H. Ye, Adv. Energy Mater. 5 (2015) 402279–402289.
[26] H. Ye, H.S. Park, A.J. Bard, J. Phys. Chem. C 115 (2011) 12464–12470.
[27] G. Zhao, S. Han, A.Z. Wang, Y.Z. Wu, M.W. Zhao, Z.P. Wang, X.P. Hao, Adv. Funct. Mater. 25 (2015) 5292–5299.
[28] K.A. Jackson, Kinetic Processes: Crystal Growth, Diffusion, and Phase Transformations in Materials, John Wiley & Sons, 2006.
[29] E.P. Nguyen, B.J. Carey, J.Z. Ou, J.V. Embden, E.D. Gaspera, A.F. Chrimes, M.J.S. Spencer, S. Zhuiykov, K. Kalantar-zadeh, T. Daeneke, Adv. Mater. 27 (2015) 6225–6229.
[30] D. Meissner, R. Memming, B. Kastening, J. Phys. Chem. 92 (1988) 3476–3483.
[31] H. Harada, T. Sakata, T. Ueda, J. Am. Chem. Soc. 107 (1985) 1773–1774.
[32] C.Y. Wang, X. Mo, Y. Zhou, Y.R. Zhu, H.T. Liu, Z.Y. Chen, J. Mater. Chem. 10 (2000) 607–608.
[33] Y.H. Sang, Z.H. Zhao, M.W. Zhao, P. Hao, Y.H. Leng, H. Liu, Adv. Mater. 27 (2015) 363–369.
[34] K.F. Mak, C. Lee, J. Hone, J. Shan, T.F. Heinz, Phys. Rev. Lett. 105 (2010) 136805–136808.
[35] M. Zirak, M. Zhao, O. Moradlou, M. Samadi, N. Sarikhani, Q. Wang, H.L. Zhang, A.Z. Moshfegh, Sol. Energy Mater. Sol. C 141 (2015) 260–269.
[36] N. Jiang, Z.L. Xiu, Z. Xie, H.Y. Li, G. Zhao, W.P. Wang, Y.Z. Wu, X.P. Hao, New J. Chem. 38 (2014) 4312–4320.